Nanoscale

RSC Publishing

REVIEW

View Article Online
View Journal | View Issue

Cite this: *Nanoscale*, 2013, **5**, 6219

Tuning the formation and functionalities of ultrafine $CoFe_2O_4$ nanocrystals *via* interfacial coherent strain

Ying-Hui Hsieh,[a] Ho-Hung Kuo,[a] Sheng-Chieh Liao,[b] Heng-Jui Liu,[a] Ying-Jiun Chen,[c] Hong-Ji Lin,[c] Chien-Te Chen,[c] Chih-Huang Lai,[b] Qian Zhan,[d] Yu-Lun Chueh[b] and Ying-Hao Chu*[a]

Received 24th January 2013
Accepted 29th April 2013

DOI: 10.1039/c3nr00413a

www.rsc.org/nanoscale

Complex oxide nanocrystals with a spinel structure show their remarkable optical, electronic, mechanical, thermal, and magnetic properties. In this study, we present a simple yet versatile strategy to grow self-assembled epitaxial $CoFe_2O_4$ nanocrystals with well-controlled size (less than 10 nm) and single orientation. $CoFe_2O_4$ nanocrystals were fabricated *via* phase separation in a $BiFeO_3$–CoF_2O_4 ultrathin film by pulsed laser deposition. The coherent strain at the $BiFeO_3$–CoF_2O_4 interface suppressed the growth of the nanocrystals regardless of substrate temperatures. This strain also resulted in the ferromagnetic anisotropy and interesting conducting behaviors of ultrafine CFO nanocrystals.

Introduction

The past decade has witnessed tremendous progress in the development of nanocrystals with controllable size, shape, and new functionalities.[1,2] Complex oxides cover a broad spectrum of intriguing functionalities due to the interplays among the lattice, charge, orbital and spin degrees of freedom and offer tremendous opportunities for next generation electronic devices.[3,4] Recently, complex oxide nanocrystals with a spinel structure, *e.g.* $CoFe_2O_4$ (CFO), $MnFe_2O_4$, and $NiFe_2O_4$, show their remarkable optical, electronic, mechanical, thermal, and magnetic properties.[5,6] These properties, a strong function of the shape, size, and crystallinity of the nanocrystals,[7–11] are exploited in technological applications like ferrofluids,[12] biomedicine,[13] and recording media.[14] However, using conventional methods to synthesize complex oxides with small size and high crystallinity is very difficult and it lacks control on the orientation and functionalities. In order to provide a fundamental understanding on these nanoparticles, an advanced growth to gain better control is crucial.

In this study, a simple yet versatile strategy to grow self-assembled epitaxial CFO nanocrystals with well-controlled size (less than 10 nm) and single orientation is demonstrated. The size, morphology, and orientation of the crystal were investigated using scanning probe microscopy (SPM) and high resolution transmission electron microscopy (HRTEM). The growth kinetics and dynamics were probed using a combination of *in situ* monitoring tool, reflective high-energy electron diffraction system (RHEED), and transmission electron microscopy (TEM). We found that the ultrafine CFO nanocrystal size (less than 10 nm) was independent of the substrate temperature due to the CFO–BFO interfacial coherent strain. Such a coherent strain at the interface resulted in the ferromagnetic anisotropy of ultrafine CFO nanocrystals and changed the local conducting behaviors of CFO nanocrystals. This study delivers a generic approach to synthesize well-controlled (size, orientation, and morphology) discrete functional spinel nanocrystals and provides a pathway to explore the fundamental properties of spinel nanocrystals.

Results and discussion

Self-assembled CFO nanocrystals were fabricated *via* phase separation of a BFO–CFO system during the PLD process. In order to study the dynamics of CFO nanocrystal formation, we *in situ* monitored the RHEED patterns during the growth process. A series of RHEED patterns in Fig. 1a shows the evolution of assembled CFO nanocrystals formed on STO (001) substrates at 700 °C with various counts of laser pulse from 0 to 200. Before the PLD process, as shown in Fig. 1a, the pattern showed diffraction stripes of the STO (001) surface structure, indicating a flat substrate surface. At early stages of the PLD process for 50 and 100 pulses, the RHEED stripes remained and implied that the assembly of CFO nanocrystals did not begin yet at these stages. When the number of the pulses was increased to more than 150, a RHEED pattern corresponding to the CFO nanocrystal started to appear, as emphasized by red circles. Continuing the PLD process up to 200 pulses, the intensity of spots in red circles was enhanced. The process was then terminated to obtain an ultrafine spinel CFO nanocrystal. The

[a]*Department of Materials Science and Engineering, National Chiao Tung University, Hsinchu 30010, Taiwan. E-mail: yhc@nctu.edu.tw*

[b]*Department of Materials Science and Engineering, National Tsing Hua University, Hsinchu 30013, Taiwan*

[c]*National Synchrotron Radiation Research Center, Hsinchu 30076, Taiwan*

[d]*Department of Materials Physics and Chemistry, University of Science and Technology Beijing, Beijing 100083, China*

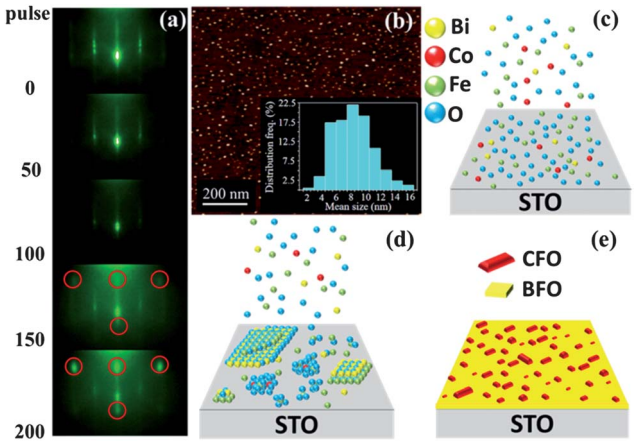

Fig. 1 *In situ* monitoring and illustration of CFO nanocrystal evolution during PLD. (a) A series of RHEED patterns showing the evolution of ultrathin CFO nanocrystals on a STO substrate at 700 °C by PLD with counts of laser pulse from 0 to 200, (b) an SPM image revealing a high density of CFO nanocrystals with a mean size of 8 nm (700 °C, 200 pulses), and the nanocrystal evolution is illustrated in (c)–(e).

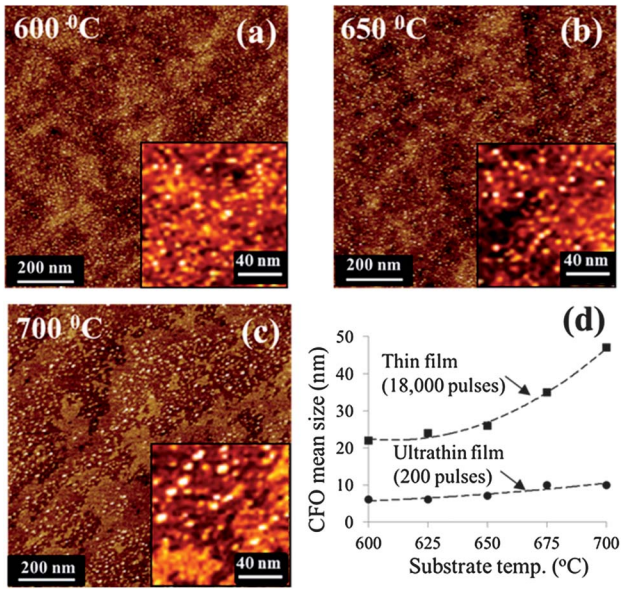

Fig. 2 Effect of STO substrate temperature on CFO nanocrystal evolution. (a–c) SPM images of ultrathin CFO nanocrystals (200 pulses) on the STO substrate at 600–700 °C, and (d) relationships of the CFO nanocrystal mean size and substrate temperature for a thin film (18 000 pulses) and an ultrathin film (200 pulses).

topography of the CFO nanocrystals was examined using AFM (Fig. 1b), and the mean size (or diameter) of 1000 CFO nanocrystals was statistically measured to be 8 nm. The visibility of only CFO spots in the RHEED pattern indicates an extrusive geometry of the CFO nanocrystals. Therefore, the evolution of the RHEED pattern clearly demonstrates the phase formation of CFO nanocrystals. We also found that the number of laser pulses needed to trigger the formation of nanocrystals does not depend on the growth rate, implying that the formation of CFO nanopillars is a nucleation-controlled process.

Based on the above results the evolution of ultrafine CFO nanocrystals is visually illustrated in Fig. 1c–e. Four species, including Bi, Co, Fe, and O, are considered to be ionized or dissociated from a BFO–CFO target by laser ablation. These atoms are then stoichiometrically transferred to the STO substrate which formed a BFO–CFO film with thickness of several unit cells, as shown in Fig. 1c. As long as the PLD process is continued, as illustrated in Fig. 1d, the phase separation can be driven in this film due to high immiscibility between spinel CFO and perovskite BFO crystals. Due to the surface energy consideration,[15] CFO crystals start their growth as the critical size (or critical radius) is reached. Consequently, a high density of single-crystalline spinel CFO nanocrystals with a polygonal morphology is coherently decomposed, as seen in Fig. 1e.

In order to explore the kinetics of the formation of CFO nanocrystals, we perturbed the system with various substrate temperatures. Morphologies of ultrafine CFO nanocrystals at different substrate temperatures were examined by AFM and are shown in Fig. 2a–c. Fig. 2d shows the effect of substrate temperature on mean size (or diameter) of 200 pulses and 18 000 pulses. The CFO nanocrystal size with 200 laser pulses for all temperatures (600–700 °C) was measured to be about 8 nm. It is interesting that increasing the substrate temperature does not increase the CFO crystal size. However, increasing laser pulses can increase the CFO nanocrystal size exponentially.

The size independence of ultrafine CFO nanocrystals as a function of substrate temperature can be attributed to the CFO–BFO interfacial coherency strain. Owing to large difference between the lattice parameter of spinel CFO ($a_0 \sim 8.391$ Å) and perovskite BFO ($a_0 \sim 3.96$ Å), the coherent strain at the CFO–BFO interface should increase dramatically when ultrafine CFO nanocrystals are coherently assembled and embedded in a BFO matrix. Such an interfacial coherent strain would impede the CFO nanocrystal growth. As the CFO nanocrystal size is increased *via* thicker film deposition, the dislocations are introduced into the CFO–BFO interface to release coherency strain. Without strain to impede growth, the CFO nanocrystal size becomes sensitive to the substrate temperature. We have used XRD to calculate the lattice parameters of $a = b = 8.384$ Å and $c = 8.369$ Å for a 8 nm CFO nanocrystal, and $a = b = 8.379$ Å and $c = 8.370$ Å for a 70 nm one. Assuming biaxial strain exist in CFO nanocrystals, the a and b components are defined as the in-plane (IP) and c as the out-of-plane (OOP) parameter. As regarding the 70 nm CFO nanocrystal as a strain free reference, the 8 nm CFO nanocrystal has longer IP and shorter OOP parameters. In other words, the 8 nm CFO nanocrystal has tensional and compressive strains existing on IP and OOP orientations, respectively.

In order to verify the proposed mechanism, a TEM study has been carried out. In our previous work,[16] we have investigated a cross-sectional high-resolution TEM image of the BFO–CFO (CFO > 70 nm) interface with the incident beam along [110] direction. We found that an edge dislocation is introduced into the BFO–CFO interface in every 20 planes in order to accommodate a high misfit strain. This semicoherent interface with dislocations was typically found in this kind of interface for the samples with CFO nanocrystals larger than 70 nm. However,

such relaxation behavior is not expected in ultrafine CFO nanocrystals since the crystal size is less than the length of 20 CFO planes. We have tried our best to acquire the information on ultrafine CFO nanocrystals (<8 nm) *via* investigation of cross-sectional TEM, unfortunately, the crystals are very tiny and are very sensitive to the electron beam, causing damage to the ultrafine CFO nanocrystals. Alternatively in the present work, we used HRTEM to investigate the plane view of ultrafine CFO micrographs. As shown in Fig. 3a, a high density of ultrafine CFO nanocrystals was uniformly grown and assembled in a BFO matrix on the STO substrate. The lattice image shows a CFO nanocrystal having a polygonal morphology. According to the identification of the diffraction pattern acquired from the lattice image by Fast Fourier transform (FFT), the zone axis is parallel to [001] of the spinel structure, and diffraction spots are contributed by its {220} and {040} facet groups. After image processing, *i.e.* filtering background noise and reverse FFT (RFFT), the lattice image clearly reveals that during the very early stage of CFO nanocrystal formation atom diffusion occurred along with directions perpendicular to the normal of {220} close-packed planes, as indicated by black arrows. Therefore, the growth rate of the {400} group is faster than {220}. Such growth behavior is well-known as the ledge mechanism of precipitation, which results in CFO nanocrystals possibly having a 2D rectangular-like shape in an ultrathin film or forming 3D nanopillars in a thicker film.[17] The lattice image of the other CFO nanocrystal in Fig. 3a and its corresponding strain mapping with the ε_{yy} component of the strain tensor are shown in Fig. 3b. The well-defined fringe in the lattice image is a prerequisite for applying geometric phase analysis (GPA) to calculate the strain field.[18] Practically, the only requirement for the image for GPA is that there should be at least two identifiable diffraction spots in the lattice image. By choosing two independent sets of lattice fringes, the 2-D strain field can be calculated. The strain mapping is represented using color bars to show the strain range from −0.5 to 0.5%. The red shift showing a positive value is defined as tensional strain; the blue shift (negative value) the compressive strain. The 1-D strain profile across the 7 nm-sized CFO nanocrystal of the 2-D mapping has been measured and is shown in Fig. 3. It can be seen that when the misfit is present at the CFO–BFO interface, the coherency strain arises at the vicinity of the boundary, either the tensional strain (red shift) or the compressive strain (blue shift). The 1-D strain profile also presents that the strain at the CFO–BFO interface (positions at 0 and 7 nm) is higher than in the interior of CFO nanocrystals. In addition, it shows the overall tensional strain present in the interior of CFO nanocrystals. In the present work, we would like to define the zone axis of this CFO nanocrystal lattice image as the out-of-plane (OOP) direction, and the directions lie on the image (or perpendicular to the zone axis) as the in-plane (IP) direction. Then, it can be understood that during the ultrathin CFO nanocrystal assembly in perovskite BFO, the misfit between them resulted in the compressive strain along with the OOP direction and eventually led to the tensional strain on in-plane (IP) directions for CFO nanocrystals.

The magnetic structure and properties of CFO nanocrystals were examined using X-ray absorption spectroscopy, X-ray magnetic circular dichroism (XMCD), and superconducting quantum interference device (SQUID) magnetometer, as shown in Fig. 4. Fig. 4a displays the Co-$L_{2,3}$ XAS spectrum of CFO nanocrystals and CoO serves as the reference for the octahedral-site (Oct.) Co^{2+}. The lowest-energy peak at 777.4 eV and the

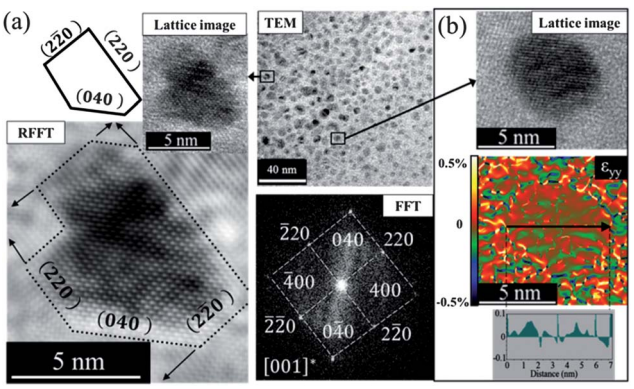

Fig. 3 (a) TEM micrographs and image processing including Fast Fourier transform (FFT) and reverse FFT (RFFT) of ultrathin CFO nanocrystals by PLD (200 pulses, 700 °C). (b) Lattice image and corresponding strain mappings (ε_{yy}) of the other nanocrystal in (a).

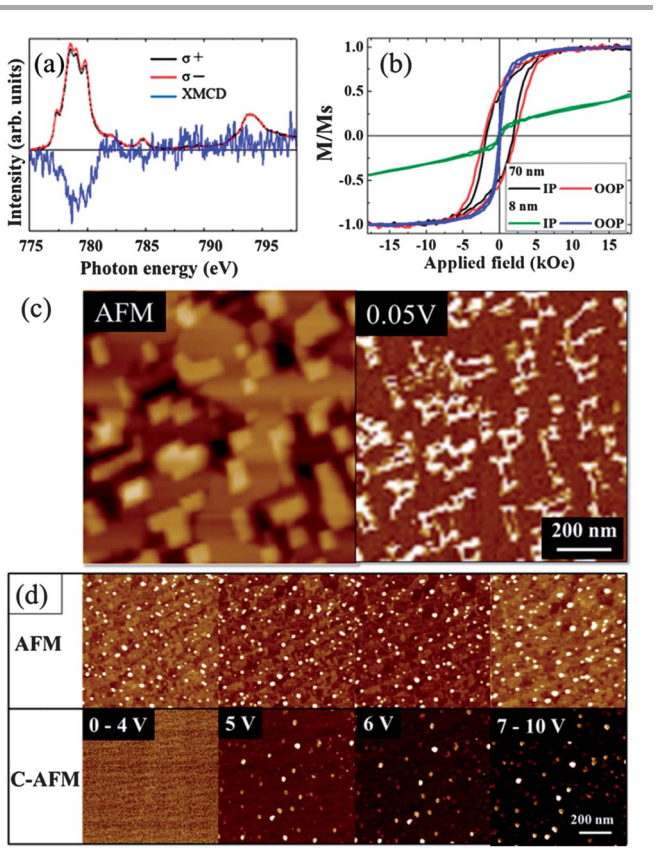

Fig. 4 (a) XAS and XMCD spectra on the Co-$L_{2,3}$ edge, and (b) the magnetic hysteresis loops, including in-plane (IP) and out-of-plane (OOP), of 8 nm- and 70 nm-sized CFO nanocrystals, respectively. The XMCD signal was normalized to the XAS intensity. AFM and C-AFM images at various applied bias of (c) large and (d) ultrafine CFO nanocrystals.

profile of μ_+ and μ_- at the Co-$L_{2,3}$ edge are the characteristics of the octahedral-site Co^{2+}. These observations strongly suggest the presence of Co^{2+} cations in this material, which is highly consistent with the results of thin film $CoFe_2O_4$.[19] Furthermore, the XMCD intensity at the L_3 edge is about ~3.3%, indicating that a magnetic moment indeed exists at the Co ion site. Such a result indicates that the CFO nanocrystal is the source of the magnetic signal. The in-plane (IP) and out-of-plane (OOP) hysteresis loops of 8 nm- and 70 nm-sized CFO nanocrystals measured by SQUID are shown in Fig. 4b. It should be noticed that the coercivity is degraded from 2000 to 100 Oe as the CFO nanocrystal size is decreased from 70 to 8 nm. Rondinone *et al.*[20] found that the blocking temperature of a 12 nm-sized CFO nanoparticle is measured at 320 K (47 °C). The blocking temperature is proportional to the volume of magnetic particles. Therefore, in the present work, the total magnetic anisotropy energy of 8 nm-sized CFO nanocrystals is approximated to be 100 K. It implies that the superparamagnetic relaxation would suppress coercivity at room temperature. Cullity and Graham[21] gave the same conclusion that degradation of coercivity is attributed to the superparamagnetic relaxation.

It is also of interest that magnetism of 8 nm-sized CFO nanocrystals emerged as an anisotropic feature. For instance, when the applied field was up to 1.5 Tesla the magnetic field was measured to be 0.4 for the IP curve and 1.0 for the OOP loop. Such a magnetic anisotropy is not present in 70 nm-sized CFO nanocrystals. As mentioned above, when the CFO nanocrystal size is small enough, a coherency strain is induced at the CFO–BFO interface. The magnetic anisotropy could be attributed to the interfacial strain. In addition, the negative value of the magnetostriction coefficient implies that magnetic moment would prefer to lie parallel to the direction of compressive stress.[22] As shown in Fig. 3b, the tensional strain is distributed on the IP directions, *i.e.* the IP strain is dominated by tensional, and the compressive strain is then induced at the OOP direction. Owing to this strain behavior, the magnetic anisotropy of ultrafine CFO nanocrystals (8 nm) is observed. Dislocation would be induced to release the interfacial coherency strain as the CFO nanocrystal size is increased.[23] Therefore, the magnetic anisotropy is not observed in 70 nm-sized CFO nanocrystals due to their large size having free coherent strain but higher density of interfacial dislocation.

AFM and C-AFM images at various applied bias of large and ultrafine CFO nanocrystals are shown in Fig. 4c and d. It should be noticed first in Fig. 4c that the conductive area of large CFO nanocrystals is revealed at the vicinity of the CFO–BFO interface after applying 0.05 V of bias. During the CFO nanocrystal growth, dislocation was introduced into the moving interface, by which the interfacial coherent strain was released. Radzimski *et al.*[24] proposed that misfit dislocation is beneficial to defect-induced conductivity of electronic devices. Evstropov *et al.*[25] and Belyaev *et al.*[26] showed that the current flow in the III–V heterojunctions is generally governed by multistep tunneling with the involvement of dislocations even at room temperature. Therefore, it can be concluded that the interfacial misfit dislocation can be regarded as an easy way for electron transportation. When the bias is applied to the large CFO nanocrystals, the electron prefers to move along the CFO–BFO interface rather than the interior of large CFO nanocrystals. As the size is controlled to be small enough, as seen in Fig. 4d, the conductive area is revealed to concentrate at the interior of ultrafine CFO nanocrystals when the bias applied is up to 5 V. The conductivity remains stable even when the bias is increased to 10 V. Fig. 3b shows that the interfacial coherent strain is higher than the interior strain of an ultrafine CFO nanocrystal; the higher the strain the higher the resistance to electron transportation. It can be interpreted that owing to higher interfacial coherent strain, the electron prefers to move along the interior of ultrafine CFO nanocrystals rather than along the CFO–BFO interface.

Experimental section

CFO nanocrystals were fabricated *via* phase separation in a $BiFeO_3$–CoF_2O_4 (BFO–CFO) ultrathin film by pulsed laser deposition (PLD) with a 248 nm KrF laser.[27] The composite target is made of 65% BFO and 35% CFO (molar ratio) and $SrTiO_3$ (001) is used as a substrate. Thin films were deposited on the STO substrate at different substrate temperatures (600–700 °C) in 200 mTorr of O_2 pressure. The CFO evolution in the growth process was monitored *in situ* with reflective high energy electron diffraction (RHEED).[28] Topographical examinations were studied by means of atomic force microscopy (AFM) using a Veeco EnviroScope. Conductive AFM (C-AFM) at various bias ranging from 0 to 10 V applied to the sample was also conducted to measure the conducting behavior of CFO nanocrystals. TEM plane-view foil was prepared by grinding the sample from the STO substrate side, and then fixed on a 3 mm Cu O-ring for further ion-milling process to decrease the thickness of foil to less than 100 nm. The foil was investigated using a TEM (JEOL-2010) with a LaB_6 thermal gun accelerated in 200 kV. Image processing, including Fast Fourier transform (FFT) and reverse FFT (RFFT), was conducted using commercial software (DigitalMicrograph) to obtain a high-quality lattice image. Geometric phase analysis (GPA) was performed to calculate strain mapping of the lattice image using free software named FRWRtools developed by the Electron and Ion Microscopy group at Ulm University, Germany. The magnetic hysteresis loops were characterized with applied fields up to 7 Tesla by means of a magnetic property measurement system (MPMS, Quantum Design Co. Ltd.) utilizing superconducting quantum interference device (SQUID) technology.

Conclusions

Self-assembled ultrafine CFO spinel nanocrystals have been successfully fabricated *via* phase separation of BFO–CFO during the PLD process on a $SrTiO_3$ (001) substrate. We found that the ultrafine CFO nanocrystal size (less than 10 nm) was independent of the substrate temperature. It is attributed to the crystal growth suppression by the CFO–BFO interfacial coherent strain. Such a coherent strain at the interface resulted in the ferromagnetic anisotropy of ultrafine CFO nanocrystals and changed the local conducting behaviors of CFO nanocrystals. This study

paves a way to control the formation and tune the functionalities of spinel nanocrystals.

Acknowledgements

This work is supported by the National Science Council, R.O.C (NSC-101-2119-M-009-003-MY2), Ministry of Education (MOE-ATU 101W961), and Center for Interdisciplinary Science of National Chiao Tung University. This work is also supported by the National Natural Science Foundation of China with Grant no. 50971015.

Notes and references

1 C. T. Campbell, *Science*, 2004, **306**, 234.
2 J. P. Juste, I. P. Santos, L. M. L. Marzan and P. Mulvaney, *Coord. Chem. Rev.*, 2005, **249**, 1870.
3 H. Takagi and H. Y. Hwang, *Science*, 2010, **327**, 1601.
4 J. Mannhart and D. G. Schlom, *Science*, 2010, **327**, 1607.
5 K. Yamaura, Q. Z. Huang, L. Q. Zhang, K. Takada, Y. Baba, T. Nagai, Y. Matsui, K. Kosuda and E. T. Muromachi, *J. Am. Chem. Soc.*, 2006, **128**, 9448.
6 M. V. Kovalenko, M. I. Bodnarchuk, R. T. Lechner, G. Hesser, F. Schäffler and W. F. Heiss, *J. Am. Chem. Soc.*, 2007, **129**, 6352.
7 R. F. Service, *Science*, 1996, **271**, 920.
8 V. F. Puntes, K. M. Krishnan and A. P. Alivisatos, *Science*, 2001, **291**, 2115.
9 A. N. Goldstein, C. M. Echer and A. P. Alivisatos, *Science*, 1992, **256**, 1425.
10 A. P. Alivisatos, *Science*, 1996, **271**, 933.
11 M. A. El-Sayed, *Acc. Chem. Res.*, 2004, **37**, 326.
12 V. Corral-Flores, D. Bueno-Baqués and R. F. Ziolo, *Acta Mater.*, 2010, **58**, 764.
13 D. P. Tang, R. Yuan, Y. Q. Chai and H. Z. An, *Adv. Funct. Mater.*, 2007, **17**, 976.
14 Q. Dai, D. Berman, K. Virwani, J. Frommer, P. O. Jubert, M. Lam, T. Topuria, W. Imaino and A. Nelson, *Nano Lett.*, 2010, **10**, 3216.
15 H. M. Zheng, Q. Zhan, F. Zavaliche, M. Sherburne, F. Straub, M. P. Cruz, L. Q. Chen, U. Dahmen and R. Ramesh, *Nano Lett.*, 2006, **6**(7), 1401.
16 Y. H. Hsieh, J. M. Liou, B. C. Huang, C. W. Liang, Q. He, Q. Zhan, Y. P. Chiu, Y. C. Chen and Y. H. Chu, *Adv. Mater.*, 2012, **33**, 4564.
17 H. Zheng, F. Straub, Q. Zhan, P. L. Yang, W. K. Hsieh, F. Zavaliche, Y. H. Chu, U. Dahmen and R. Ramesh, *Adv. Mater.*, 2006, **18**, 2747.
18 M. J. Hÿtch and T. Plamann, *Ultramicroscopy*, 2011, **87**, 199.
19 J. A. Moyer, C. A. F. Vaz, D. A. Arena, D. Kumah, E. Negusse and V. E. Henrich, *Phys. Rev. B: Condens. Matter Mater. Phys.*, 2001, **84**, 054447.
20 A. J. Rondinone, A. C. S. Samia and Z. J. Zhang, *J. Phys. Chem. B*, 1999, **103**, 6876.
21 B. D. Cullity and C. D. Graham, *Introduction to Magnetic Materials*, John Wiley & Sons, Inc., Hoboken, New Jersey, 2009, 362.
22 R. M. Bozorth, E. F. Tilden and A. J. Williams, *Phys. Rev. B: Solid State*, 1955, **99**, 1788.
23 Q. Zhan, R. Yu, S. P. Crane, H. Zheng, C. Kisielowski and R. Ramesh, *Appl. Phys. Lett.*, 2006, **89**, 172902.
24 Z. J. Radzimski, T. Q. Zhou, A. B. Buczkowski and G. A. Rozgonyi, *Appl. Phys. A: Solids Surf.*, 1991, **53**, 189.
25 V. V. Evstropov, M. Dzhumaeva, Y. V. Zhilyaev, N. Nazarov, A. A. Sitnikova and L. M. Fedorov, *Semiconductors*, 2000, **34**(11), 1357.
26 A. E. Belyaev, N. S. Boltovets, V. N. Ivanov, V. P. Klad'ko, R. V. Konakova, Y. Y. Kudrik, A. V. Kuchuk, V. V. Milenin, Y. N. Sveshnikov and V. N. Sheremet, *Semiconductors*, 2008, **42**, 689.
27 H. Zheng, J. Wang, S. E. Lofland, Z. Ma, L. Mohaddes-Ardabili, T. Zhao, L. Salamanca-Riba, S. R. Shinde, S. B. Ogale, F. Bai, D. Vieland, Y. Jia, D. G. Schlom, M. Wuttig, A. Roytburd and R. Ramesh, *Science*, 2004, **30**, 661.
28 S. C. Liao, P. Y. Tsai, C. W. Liang, H. J. Liu, J. C. Yang, S. J. Lin, C. H. Lai and Y. H. Chu, *ACS Nano*, 2011, **5**, 4118.